Article

Two-Dimensional Perovskite/HfS$_2$ van der Waals Heterostructure as an Absorber Material for Photovoltaic Applications

Deobrat Singh* and Rajeev Ahuja*

ACCESS | Metrics & More | Article Recommendations | SI Supporting Information

ABSTRACT: Van der Waals (vdW) heterostructures of perovskites and transition metal dichalcogenides (TMDCs) have attracted increased interest owing to their extraordinary optoelectronic properties and encouraging applications. Two-dimensional (2D) TMDCs, i.e., hafnium disulfide (HfS$_2$), are also interesting because of their unique optoelectronic properties. Therefore, the combination of these different types of materials is very smart in terms of the fundamental science of interface interaction, as well as for the understanding of ultrathin optoelectronic devices with superior performance. Here, we have systematically modeled the 2D CH$_3$NH$_3$PbI$_3$/HfS$_2$ vdW heterostructure by using first-principles calculations. The substituted interface has enhanced visible-light sensitivity and photoelectrocatalytic activity by reducing the transition energies. The interfacial interaction of both materials effectively tunes the band gap of the interface; therefore, it would significantly improve the photoreactivity for solar cell applications. Due to the presence of small effective masses of electrons−holes, high optical absorption on the order of 10^5 and high spectroscopic limited maximum efficiency of 28.45% in the CH$_3$NH$_3$PbI$_3$/HfS$_2$ vdW heterostructure will be better candidates in the field of absorber materials. The considered systems are expected to be more efficient in separating the photogenerated electrons−holes and active in the visible spectrum. These theoretical results suggest that the CH$_3$NH$_3$PbI$_3$/HfS$_2$ vdW heterostructure may lead to many novel applications in efficient light-absorbing materials for photovoltaic applications.

KEYWORDS: 2D perovskite/HfS$_2$ vdW heterostructure, electronic properties, charge transfer mechanism, optical properties, spectroscopic limited maximum efficiency (SLME)
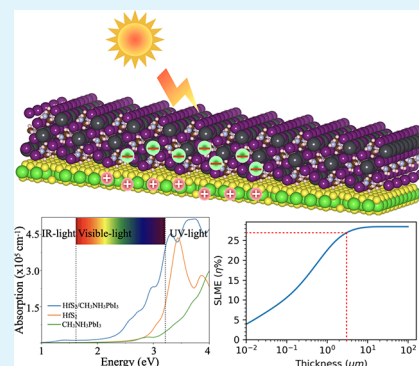
■ INTRODUCTION

Nowadays, hybrid organic−inorganic lead halide perovskites have greatly attracted interest toward photovoltaic absorber materials due to their remarkable optoelectronic properties such as high optical absorption spectra in the visible region, tunable band gap, and long electron−hole diffusion lengths.[1−3] These interesting properties are very useful in solar cells, and it is reported that the power conversion efficiency has been significantly enhanced in the lead halide perovskites-based solar cells in the past few years along with their values of 22.7%. Apart from this, there are several more applications of CH$_3$NH$_3$PbI$_3$ perovskites such as light-emitting diodes, lasers, and photodetectors.[4−6] The general chemical formula of organic−inorganic perovskites is ABX$_3$ where A = CH$_3$NH$_3^+$, B = Pb^{2+}, Sn^{2+}, and X = halide elements in which the highly studied perovskite structure is methylammonium lead iodide perovskite (CH$_3$NH$_3$PbI$_3$), and it displayed a high optical absorption coefficient on the order of 10^5 cm^{-1}, long carrier diffusion length of 100 μm, and radiative efficiency exceeding 90%.[7−9]

Recently, the 2D sheet of CH$_3$NH$_3$PbI$_3$ perovskites was synthesized experimentally, and they found that the 2D CH$_3$NH$_3$PbI$_3$ perovskites have larger exciton binding energy, higher photoluminescence quantum yield (PLQY) than bulk counterparts due to the quantum confinement effect.[10−13]

Additionally, a tunable electronic band gap can be controlled by increasing/decreasing the thickness of 2D CH$_3$NH$_3$PbI$_3$ perovskites.[10,14] Accordingly, the preparation of the heterostructure of 2D perovskites with the other 2D layered materials is expected to provide a new exciting phenomenon and to explore the physical/chemical properties of the individual constituents. 2D monolayers of semiconducting transition metal dichalcogenides (TMDCs) are the best favorable candidates for optoelectronic properties, for example, molybdenum disulfide (MoS$_2$), tungsten disulfide (WS$_2$), and hafnium disulfide (HfS$_2$).[15−17] Some of the TMDC monolayers have direct band gaps in the visible region such as MoS$_2$, WS$_2$, MoSe$_2$, WSe$_2$, MoTe$_2$, etc.; whereas the TMDC HfS$_2$ monolayer displayed the indirect band gap, and it contains a three atom thick layered 2D structure.[18,19] The TMDC 2D 1T-HfS$_2$ monolayer shows exciting electronic and optical properties.[19] Additionally, the 1T-HfS$_2$ monolayer has a direct band gap of
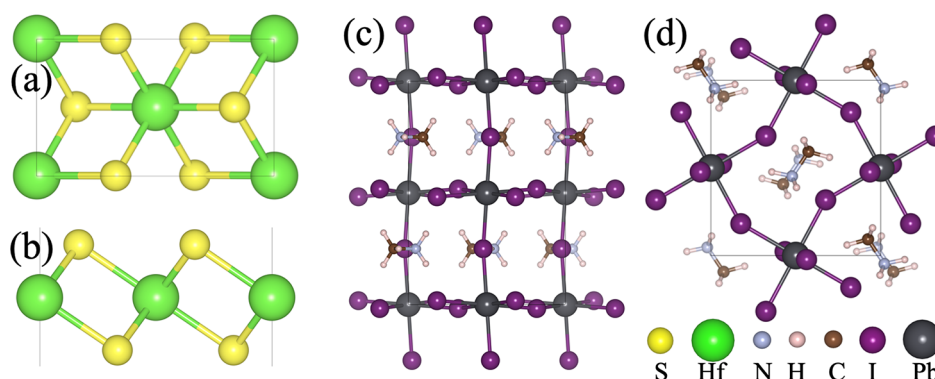
Figure 1. Fully optimized structures of the 2D 1T-HfS$_2$ monolayer with (a) top and (b) side views. The optimized structure of the CH$_3$NH$_3$PbI$_3$ perovskite with (c) top and (d) side views. The atomic representations are presented by spherical balls at the bottom of Figure 1(d).

1.29 eV,[20] and it shows other promising properties such as ultrahigh room temperature carrier mobility, chemical stability, mechanical flexibility, sheet current density, and reasonable band gap.[19,21] Due to these exciting properties of the 1T-HfS$_2$ monolayer, it is a very useful application in the fields of photocatalyst, field-effect transistors, photodetectors, phototransistor, and thermoelectric.[19,22,23]

Generally, heterostructure materials displayed relatively superior electronic, interfacial, and optical properties with respect to the layers of individual materials.[24] The interfacial charge transfer mechanism in heterostructure materials depends on some physical/chemical parameters, for example, surface behavior, interfacial characteristics, their band edge alignments, and charge carrier mobility.[24] Recently, it was found that the CH$_3$NH$_3$PbI$_3$/TiO$_2$ heterostructure significantly enhanced the optical absorption strength in the visible region and photoelectrocatalytic mechanism. Also, interfaces of the heterostructure are more efficient in separation of the photogenerated electron−hole.[25] It was also reported that the CH$_3$NH$_3$PbI$_3$/TiO$_2$ heterostructure shows an electric power conversion efficiency (PCE) of 7.3% for photovoltaic cells.[26] In addition, the CH$_3$NH$_3$PbI$_3$/WS$_2$ heterostructure has been investigated for high performance ultrathin optoelectronic devices.[27] Apart from this, the CH$_3$NH$_3$PbI$_3$/MoS$_2$ heterostructure was demonstrated for ultrafast charge transfer at the interface,[28] and it was also reported that it displayed a high PCE of 18.31% which will be very useful for stable photovoltaic devices.[29] There are several other perovskites/TMDC heterostructures that were demonstrated for various device performances.[30−33]

Motivated by these interesting works on perovskites/TMDC heterostructures, we have selected the CH$_3$NH$_3$PbI$_3$/HfS$_2$ heterostructure. In the present work, we mainly focused on the structural, electronic, and optical properties and charge transfer mechanism at the interface of a CH$_3$NH$_3$PbI$_3$/HfS$_2$ vdW heterostructure using first-principles calculations based on Density Functional Theory (DFT). When the CH$_3$NH$_3$PbI$_3$ material is placed on the surface of the HfS$_2$ material, then the band edges of both materials are altered accordingly, and it forms a semiconductor−semiconductor heterostructure. The work function analysis showed that the CH$_3$NH$_3$PbI$_3$/HfS$_2$ vdW heterostructure lies between the pristine HfS$_2$ and CH$_3$NH$_3$PbI$_3$ structures; therefore, redistribution of charge occurs in the whole structure, and some of the charge transfer occurs at the interface due to it generating an internal electric field. Further, optical properties of the CH$_3$NH$_3$PbI$_3$/HfS$_2$ vdW heterostructure have high optical absorption in the visible region as compared to the pristine HfS$_2$ and CH$_3$NH$_3$PbI$_3$ structures.

Also, we have investigated the spectroscopic limited maximum efficiency (SLME) of the CH$_3$NH$_3$PbI$_3$/HfS$_2$ vdW heterostructure. Due to the presence of strong optical absorption in the visible region, the high value of SLME shows it is a very superior candidate for photocatalytic and photovoltaic applications.

■ COMPUTATIONAL METHODS

The electronic structure calculations are based on the projected augmented wave (PAW) pseudopotential[34] applied to describe the interactions between core and valence electrons as implemented in the Vienna *Ab initio* Simulation Package (VASP) code.[34,35] The Perdew−Burke−Ernzerhof (PBE)[36] functional is used to describe the exchange-correlation interactions. To describe the van der Waals (vdW) interactions between the HfS$_2$ and CH$_3$NH$_3$PbI$_3$ interface, we have used Grimme's D3 dispersion correction (DFT-D3).[37] To get the accurate electronic band gap, we have used the hybrid HSE06 functional[38] with a screening parameter (μ) of 0.2 Å^{-1} and mixing parameter (α) of 25%. To prevent the physical interaction between the periodic image, we have selected 15 Å thick along the *z*-direction. An energy cutoff of 500 eV is used to describe the valence electrons for the plane-wave basis set. The conjugate-gradient (CG) algorithm is used during the structural optimization, and ions are fully relaxed until the residual force on each atom is less than 10^{-3} eV/Å. For self-consistent field (SCF) calculations, the energy convergence criteria are set as 1 × 10^{-6} eV. The k-point meshes with the Monkhorst−Pack scheme is sampled by 15 × 15 × 1 for the 1T-HfS$_2$ monolayer, 6 × 8 × 6 for the CH$_3$NH$_3$PbI$_3$ perovskite, and 2 × 3 × 1 for the CH$_3$NH$_3$PbI$_3$/HfS$_2$ vdW heterostructure which were employed for the electronic structure calculations. The Bader charge approach is employed[39] to see the charge transfer mechanism between the HfS$_2$ and CH$_3$NH$_3$PbI$_3$ interface.

Further, to calculate the structural mismatch, we have chosen the (5 × 2 × 1) supercell of the 1T-HfS$_2$ monolayer and the (2 × 1 × 1) supercell of the CH$_3$NH$_3$PbI$_3$ perovskite, and it is calculated by the following relation

$$\Delta a = \left(\frac{|a_{HfS_2} - a_{Perovskite}|}{a_{HfS_2}} \right) \times 100 \tag{1}$$

where a_{HfS_2} and $a_{Perovskite}$ represent the lattice parameters of the HfS$_2$ monolayer and CH$_3$NH$_3$PbI$_3$ perovskite, respectively. From the above equation, the calculated lattice mismatch Δa is found to be 3.07% and 0.4% along the *a* and *b* directions, respectively, which is favorable to make the heterostructure.[40]

Also, to check the thermodynamic stability of the vdW heterostructure, we have investigated the adhesion energy, and it is represented by the following equation

$$E_{adh} = E_{Perovskite/HfS_2} - E_{Perovskite} - E_{HfS_2} \tag{2}$$

where $E_{Perovskite}$, E_{HfS_2}, and $E_{Perovskite/HfS_2}$ represent the total energy of pristine Perovskite, HfS₂, and Perovskite/HfS₂ vdw heterostructure systems, respectively. The calculated E_{adh} is found to be −10.13 eV (≈−45.47 meV/Å²) which is relatively lower than previously reported vdW heterostructures.[40,41]

■ RESULTS AND DISCUSSION

Structure and Electronic Properties of 2D 1T-HfS₂ and CH₃NH₃PbI₃ Perovskite. The optimized structures of 2D 1T-HfS₂ and the CH₃NH₃PbI₃ perovskite with top and side views are presented in Figure 1a−d. The optimized lattice constant of the 1T-HfS₂ monolayer with a rectangular unit cell is a = 3.65 Å and b = 6.32 Å, and the corresponding bond length between the Hf and S atoms is 2.54 Å which is highly consistent with previous literature.[22,23] The optimized lattice parameter of the ortho-rhombic CH₃NH₃PbI₃ perovskite is found to be a = 8.84 Å, b = 12.59 Å, and c = 8.56 Å which is good agreement with previous work.[42,43]

Further, we have investigated the orbital contributed electronic band structures and electronic density of states (DOS) for both considered materials. From the orbital contributed band structure of the 1T-HfS₂ monolayer (see Figure 2a), the top of the valence band is dominated by S p-
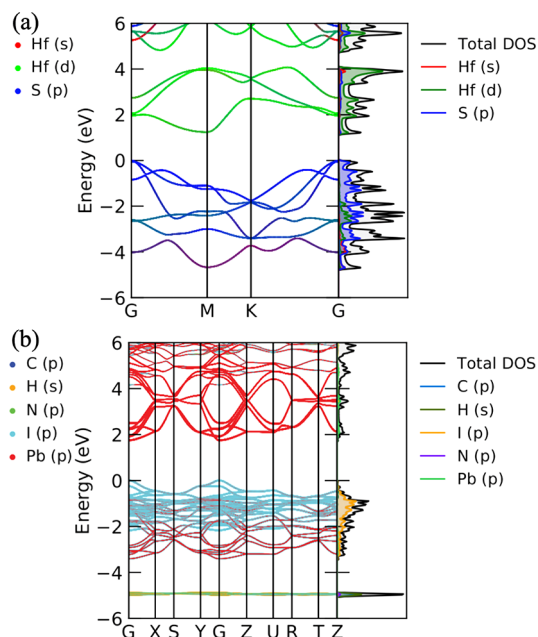
valence and conduction bands from I p-states to Pb p-states. The CH₃NH₃PbI₃ material displayed the semiconducting behaviors because valence and conduction bands are separated by 1.74 eV, and it shows a direct band gap semiconductor.

In addition, the total and projected density of states of 2D 1T-HfS₂ and the CH₃NH₃PbI₃ bulk perovskite are presented in Figure 2a,b. From Figure 2a, S p-states are mainly contributed near the Fermi level in the valence band maximum (VBM) in the electronic density of states of 1T-HfS₂, whereas conduction band minimum (CBM) is made by Hf d-states which is found in the electronic band structure. It was also seen that the small contribution comes from Hf p- and Hf d-states in VBM and S p-states in CBM. The I p-states are mainly contributed near the Fermi level in the VBM, while the Pb p-states have a higher contribution in CBM which has similar contributions that appear in the electronic band structure (see Figure 2b).

Charge Transfer Mechanism in the CH₃NH₃PbI₃/HfS₂ vdW Heterostructure. Figure 3a shows the charge density

Figure 2. Orbital contributed electronic band structures and corresponding projected density of states: (a) 2D 1T-HfS₂ monolayer and (b) CH₃NH₃PbI₃ bulk perovskite. The Fermi level is set to zero.
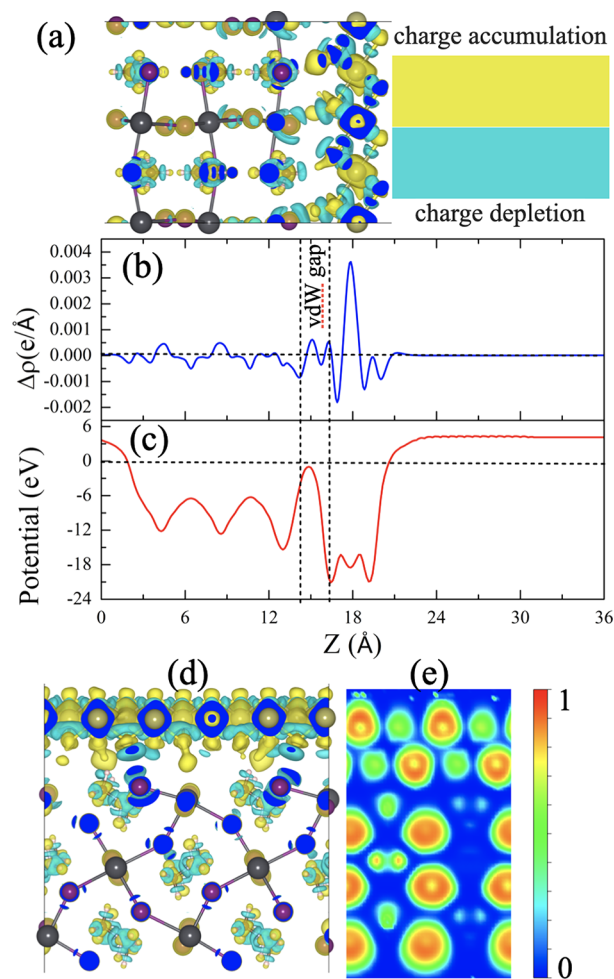
Figure 3. (a) Charge density difference plot of the CH₃NH₃PbI₃/HfS₂ vdW heterostructure and (b) planar charge density difference profile at the interface of the vdW heterostructure. The yellow and cyan colors represent the charge accumulation and charge depletion region. (c) Electrostatic potential profile of the CH₃NH₃PbI₃/HfS₂ vdW heterostructure along the z-direction. (d,e) Other orientations of the charge density difference plot and corresponding electron localized function (ELF) of the CH₃NH₃PbI₃/HfS₂ vdW heterostructure. The isosurface is set as 3 × 10⁻⁴ e/Å⁻³.

orbitals, and the bottom of the conduction band mainly originates from Hf d-orbitals. It was also seen that the Hf s-orbitals have a deep energy label in the valence band around −4 eV. It means that the interband transition first occurs from S p-states in the valence band to Hf d-states of the conduction band, and the valence and conduction bands are separated by 1.29 eV using the GGA-PBE functional (i.e., it shows a semiconducting nature with an indirect band gap) which is in good agreement with previous work.[22,23] Figure 2b shows the orbital contributed electronic band structure of the CH₃NH₃PbI₃ material. The I p-orbitals have the main contribution at the top of the valence band, whereas the conduction band is mainly made by Pb p-orbitals. Therefore, the interband transition occurs between the

difference profile of the $CH_3NH_3PbI_3/HfS_2$ vdw heterostructure which is calculated by the following equation

$$\Delta\rho = \rho_{HfS_2/CH_3NH_3PbI_3} - \rho_{HfS_2} - \rho_{CH_3NH_3PbI_3} \qquad (3)$$

where ρ_{HfS_2} is the charge density of HfS_2, $\rho_{CH_3NH_3PbI_3}$ is the charge density of $CH_3NH_3PbI_3$, and $\rho_{HfS_2/CH_3NH_3PbI_3}$ shows the charge density of the complex $CH_3NH_3PbI_3/HfS_2$ structure. The significant electron cloud is presented at the interface of the $CH_3NH_3PbI_3/HfS_2$ vdW structure (see Figure 3a,d). It means that some of the electron transfer occurred between the $CH_3NH_3PbI_3/HfS_2$ vdW structure. Figure 3 displayed the planar-averaged electron density difference profile. It was seen that the positive charge appears at the HfS_2 surface, whereas the negative charge has the $CH_3NH_3PbI_3$ surface. Therefore, we can say that the HfS_2 monolayer transfers some electrons to the $CH_3NH_3PbI_3$ surface through the vdW gap. To get the exact amount of electron transfer between the surface, we have investigated the Bader charge analysis. From the Bader charge analysis, the HfS_2 monolayer transfers 0.99 e$^-$ to the $CH_3NH_3PbI_3$ surface. The direction of electron transfer is confirmed by electrostatic potential and the corresponding work function of the considered materials (see Figure 3c). The calculated work function of the HfS_2 and $CH_3NH_3PbI_3$ structures is found to be 5.70 and 6.05 eV, respectively. When the $CH_3NH_3PbI_3$ structure is placed on the surface of the HfS_2 structure, then it is found to be 5.91 eV of the $CH_3NH_3PbI_3/HfS_2$ vdW heterostructure. This value lies between the HfS_2 and $CH_3NH_3PbI_3$ structures. Due to the presence of the 0.35 eV energy difference in electrostatic potential, it generates an internal electric field at the interfacial surface. In addition, these differences in energy displayed redistribution of charge in the vdW heterostructure. The calculated value of the work function is 5.70 eV for HfS_2 and is relatively lower as compared to the $CH_3NH_3PbI_3$ (6.05 eV) structure; therefore, the $CH_3NH_3PbI_3/HfS_2$ vdW heterostructure shows spontaneous interfacial electron transfer from HfS_2 to the $CH_3NH_3PbI_3$ side. It is well-known that charge transfer always occurs from lower potential to higher potential[40] which is found to be a similar trend in the present work. Due to the built-in electric field and significant charge transfer at the interface of the $CH_3NH_3PbI_3/HfS_2$ vdW heterostructure, it will effectively enhance the photogenerated electron (e$^-$) and hole (h$^+$) pairs, i.e., the photoexcited e$^-$ tends to distribute at the HfS_2 side, whereas h$^+$ tends to distribute at the surface of $CH_3NH_3PbI_3$. Additionally, Figure 4 displayed the band alignment of HfS_2 and
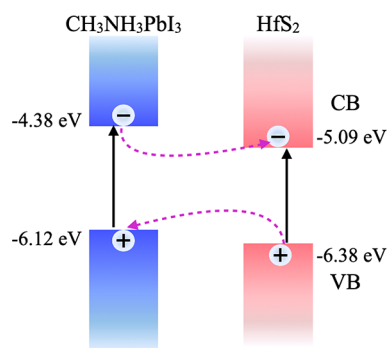
Figure 4. Schematic illustration of the type-II band alignment and charge transfer mechanism between the 2D HfS_2 monolayer and $CH_3NH_3PbI_3$ perovskite material.

$CH_3NH_3PbI_3$ perovskite materials in which valence and conduction band edges are investigated by first-principles calculations for both materials. It is confirmed that its band alignment exhibits a type-II (staggered) semiconductor. From Figure 4, it is clearly seen that the electron transfer occurs from the HfS_2 to the $CH_3NH_3PbI_3$ perovskite layer. It is reported that the type-II donor−acceptor heterointerface can easily promote the transfer of electrons and holes which effectively separate at the interface.[44] From these results, we can say that it would significantly decrease the charge carrier recombination and enhance the photocatalytic activity as well, as it will be beneficial for solar cell applications.

Further to check the chemical bonding mechanism between the HfS_2 and $CH_3NH_3PbI_3$ structures, we have investigated the electron localization function (ELF) (see Figure 3e). The different color is represented by the color map on the right side of Figure 3e in which the red color means electrons are highly localized, whereas no localization of electrons is available at the blue color side. It was seen that the Hf−S pairs are slightly localized because between the Hf−S bonds the color scheme value is around 0.5. Similar trends are found between the atomic bonds in the $CH_3NH_3PbI_3$ structure; therefore, C−H, N−H, C−N, and Pb−I pairs have slightly localized. Additionally, along the interfacial surface between the HfS_2 and $CH_3NH_3PbI_3$, there is no localization of electrons found because the color scheme is completely blue between the S−I, S−H, S−C, and S−N atoms. At the interface of the vdW heterostructure, the ELF values are smaller than ∼0.25 which confirmed the chemical bond between the interface of the $CH_3NH_3PbI_3/HfS_2$ system atoms is absent.

Optical Properties and Spectroscopic Limited Maximum Efficiency (SLME). Now, we will discuss the optical properties of the pristine 1T-HfS_2 monolayer and the bulk $CH_3NH_3PbI_3$ structure as well as the $CH_3NH_3PbI_3/HfS_2$ vdW heterostructure. The calculated optical properties such as real and imaginary parts of dielectric function, refractive index, extinction coefficient, optical absorption coefficient, and electron energy loss function as a function of photon energy which varies from 0 to 8 eV are presented in Figure S1 and Figure S2 (see the Supporting Information). Figure 5 shows the optical absorption coefficient in which the photon energy is plotted up to 4 eV. For solar cell applications, it is necessary to have high optical absorption in the visible region of the solar spectrum that occupies 45% of the whole solar spectrum range.[45] The optical absorption generally depends on the interband transition probability of the carriers from the valence and conduction bands. The dipole transition matrix element (p^2) is presented as corresponding electronic band structures of pristine 1T-HfS_2 and bulk $CH_3NH_3PbI_3$ (see Figure 5a,b). It was seen that the electronic band lines are highly dispersive VBM and CBM around G-M/G-Y and M-K/G-Y directions and have lower effective mass (see Table 1) and high electron mobility which shows low recombination rates of electrons and holes[46] for 1T-HfS_2 and bulk $CH_3NH_3PbI_3$ systems, respectively. From the orbital contributed electronic band structure, VBM is dominated by S p-orbitals, whereas CBM is dominated by Hf d-orbitals which are located around G and M points, respectively. Figure 5a for 1T-HfS_2 exhibits high transition probability located around M points; and their interband transition occurs from S p-states to Hf d-states, and relatively small transition probability is found at G points as compared to M points. It means that at that band edges, it will give reasonably high optical absorption. In the case of the bulk $CH_3NH_3PbI_3$ structure, the VBM is mainly dominated by I p-orbitals, while
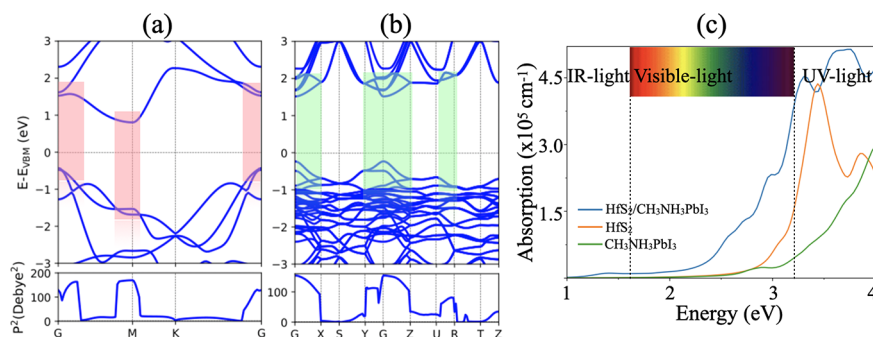
Figure 5. Electronic band structure and corresponding transition probability (p^2) of (a) the pristine 2D 1T-HfS$_2$ monolayer and (b) bulk CH$_3$NH$_3$PbI$_3$ material. The shaded region with pink and green colors in the electronic band structure represents the maximum transition probability of electrons from valence band maximum to conduction band minimum. (c) Optical absorption spectra of the pristine 1T-HfS$_2$ monolayer, bulk CH$_3$NH$_3$PbI$_3$ material, and CH$_3$NH$_3$PbI$_3$/HfS$_2$ vdW heterostructure.

Table 1. Effective Mass of Electrons (m_e^*/m_0) and Holes (m_h^*/m_0) of the Pristine 1T-HfS$_2$ Monolayer and Bulk CH$_3$NH$_3$PbI$_3$ Material

parameter	remarks	
1T-HfS$_2$		
m_h^*	0.24 (G-M)	0.30 (G-K)
m_e^*	2.40 (M-G)	0.23 (M-K)
CH$_3$NH$_3$PbI$_3$		
m_e^*	0.31 (G-X)	0.25 (G-Y)
m_h^*	0.68 (G-X)	0.09 (G-Y)

the CBM mainly originates from Pd p-orbitals and is located around G points toward the X and Y directions. It shows high interband transition probability at G points, as well as G-X and G-Y directions which appear at G and G-X/G-Y points and directions from I p-states to Pb p-states, and a small part of the interband transition occurs between U-R points from VBM to CBM (see the shaded region in Figure 5b). It means that when photon energy is incident on the CH$_3$NH$_3$PbI$_3$ surface, then high interband transition/high optical absorption occurs at those high symmetry points.

More importantly, when we make the CH$_3$NH$_3$PbI$_3$/HfS$_2$ vdW heterostructure as shown in Figure 6a, then its electronic properties are significantly changed (see Figure 6b). We have

selected the vdW heterostructure that has approximately 1.8 nm thickness in which CH$_3$NH$_3$PbI$_3$ is situated on the top side and HfS$_2$ is placed at the bottom side. The electronic band structure of the CH$_3$NH$_3$PbI$_3$/HfS$_2$ vdW heterostructure shows semiconducting behaviors with the direct band gap of 0.52 eV with the GGA-PBE functional and 1.04 eV using the hybrid HSE06 functional. From the transition probability profile, the maximum interband transition occurs between X-S and U-R points from the valence band to conduction. It means that high optical absorption is found along X-S and U-R points when photon energy is incident on the surface of the CH$_3$NH$_3$PbI$_3$/HfS$_2$ vdW heterostructure. Figure 5c shows the optical absorption on pristine HfS$_2$ and CH$_3$NH$_3$PbI$_3$ as well as its vdW heterostructure. It is clearly seen that the optical absorption enhanced significantly in the vdW heterostructure in the visible region. It means that more solar spectrum light is absorbed by the CH$_3$NH$_3$PbI$_3$/HfS$_2$ vdW heterostructure in the visible region. Therefore, it could be a promising application as a great light absorber material.

Further, we have investigated the SLME parameter for the CH$_3$NH$_3$PbI$_3$/HfS$_2$ vdW heterostructure to check the photovoltaic application. The SLME parameter for maximum achievable solar cell efficiency is calculated by using the band gap material and optical absorption coefficient. The details of the calculations (i.e., related equations) are presented in the
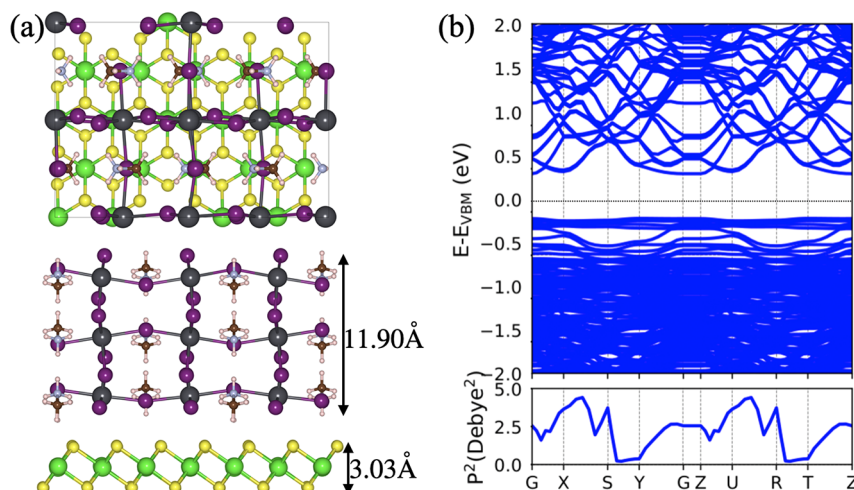

Figure 6. (a) Fully optimized structure with top and side views shows the thickness of the CH$_3$NH$_3$PbI$_3$/HfS$_2$ vdW heterostructure and (b) electronic band structure and transition probability (p^2) of the CH$_3$NH$_3$PbI$_3$/HfS$_2$ vdW heterostructure.

Supporting Information. The optimized vertical distance between the $CH_3NH_3PbI_3$/HfS$_2$ vdW heterostructure is found to be 2.77 Å, and the total thickness of materials is ~1.8 nm (see Figure 6a). We have considered the $CH_3NH_3PbI_3$/HfS$_2$ vdW heterostructure to calculate the thickness dependent SLME which is presented in Figure 7. Figure 7 shows the SLME value,

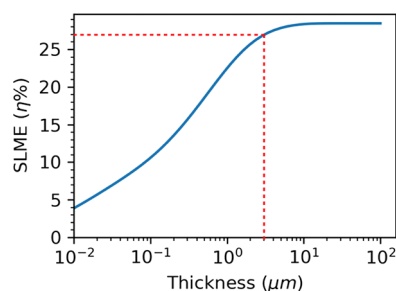**Figure 7.** Spectroscopic limited maximum efficiency (SLME) (at 298.15 K) as a function of film thickness along the best possible crystal axis of the $CH_3NH_3PbI_3$/HfS$_2$ vdW heterostructure.

as the function of film thickness varies from 0.01 to 10 μm. The SLME value increases very sharply up to 5 μm, and at 10 μm, it becomes constant. It means that when the film thickness is 10 μm, then its value is found to be 28.45%; whereas at the half film thickness of 5 μm, then its value is 27% (see the red dotted line in Figure 7) that is relatively high as compared to some of the layered materials such as AB-stacked MoGe2N4 (15.44%), 2D semiconducting tin perovskites $(CH_3(CH_2)_3NH_3)_2$-$(CH_3NH_3)_{n-1}Sn_nI_{3n+1}$ (n = 3) (24.6%), and (AEQT)SnI$_4$ in which AEQT = $H_3NC_2H_4C_{16}H_8S_4C_2H_4NH_3^{2+}$; X = Cl, Br, I (20.8%).[46−49] It means that the $CH_3NH_3PbI_3$/HfS$_2$ vdW heterostructure would be a better candidate for solar cell application. From the above investigations, the presence of high optical absorption on the order of 10^5, suitable band gap, and significantly higher SLME values confirming the $CH_3NH_3PbI_3$/HfS$_2$ vdW heterostructure will be a potential candidate for photovoltaic application.

CONCLUSIONS

We have systematically investigated structural, electronic, and optical properties of the $CH_3NH_3PbI_3$/HfS$_2$ vdW heterostructure using first-principles calculations. The $CH_3NH_3PbI_3$/HfS$_2$ vdW heterostructure displayed intrinsic properties including electronic band gaps of pristine 1T-HfS$_2$ and bulk $CH_3NH_3PbI_3$ structures which are very close to the Shockley−Queisser (SQ) limit and strong optical absorption. From work function analysis, the 1T-HfS$_2$ material has a lower work function as compared to bulk $CH_3NH_3PbI_3$ material; therefore, spontaneous electron transfer occurs from the HfS$_2$ surface to the $CH_3NH_3PbI_3$ surface which has been confirmed by the Bader charge analysis. It means that the HfS$_2$ surface has a sufficient amount of holes, whereas the $CH_3NH_3PbI_3$ surface has the same amount of electrons; therefore, it has an internal electric field which is very beneficial for photocatalytic as well as solar cell applications. In addition, the effective masses of the electrons and holes are smaller in both pristine 1T-HfS$_2$ and bulk $CH_3NH_3PbI_3$ structures due to the presence of smaller effective masses (i.e., which decrease the charge carrier recombination rate), suitable electronic band gap, high optical absorption, strong transition probability at particular high symmetry points,

and the highest value of spectroscopic limited maximum efficiency confirming its potential for photovoltaic application.

ASSOCIATED CONTENT

ⓈI Supporting Information

The Supporting Information is available free of charge at https://pubs.acs.org/doi/10.1021/acsaem.1c03796.

Computational details of optical properties and SLME; real and imaginary part of complex dielectric function and refractive index, extinction coefficient, absorption coefficient, and electron energy loss-function of pristine 1T-HfS$_2$ monolayer, $CH_3NH_3PbI_3$ perovskite, and $CH_3NH_3PbI_3$/HfS$_2$ vdw heterostructure (PDF)

AUTHOR INFORMATION

Corresponding Authors

Deobrat Singh − *Condensed Matter Theory Group, Materials Theory Division, Department of Physics and Astronomy, Uppsala University, 75120 Uppsala, Sweden;* ⓞ orcid.org/0000-0001-7246-8743; Email: deobrat.singh@physics.uu.se

Rajeev Ahuja − *Condensed Matter Theory Group, Materials Theory Division, Department of Physics and Astronomy, Uppsala University, 75120 Uppsala, Sweden; Department of Physics, Indian Institute of Technology Ropar, Rupnagar 140001 Punjab, India;* ⓞ orcid.org/0000-0003-1231-9994; Email: rajeev.ahuja@physics.uu.se

Complete contact information is available at:
https://pubs.acs.org/10.1021/acsaem.1c03796

Notes

The authors declare no competing financial interest.

REFERENCES

(1) Stranks, S. D.; Snaith, H. J. Metal-halide perovskites for photovoltaic and light-emitting devices. *Nature Nanotechnol.* **2015**, *10*, 391−402.

(2) Erkılıç, U.; Solís-Fernández, P.; Ji, H. G.; Shinokita, K.; Lin, Y.-C.; Maruyama, M.; Suenaga, K.; Okada, S.; Matsuda, K.; Ago, H. Vapor phase selective growth of two-dimensional perovskite/WS2 heterostructures for optoelectronic applications. *ACS Appl. Mater. Interfaces* **2019**, *11*, 40503−40511.

(3) Jung, H. S.; Park, N.-G. Perovskite solar cells: from materials to devices. *small* **2015**, *11*, 10−25.

(4) Kim, H.; Zhao, L.; Price, J. S.; Grede, A. J.; Roh, K.; Brigeman, A. N.; Lopez, M.; Rand, B. P.; Giebink, N. C. Hybrid perovskite light emitting diodes under intense electrical excitation. *Nat. Commun.* **2018**, *9*, 4893.

(5) Xing, G.; Mathews, N.; Lim, S. S.; Yantara, N.; Liu, X.; Sabba, D.; Grätzel, M.; Mhaisalkar, S.; Sum, T. C. Low-temperature solution-processed wavelength-tunable perovskites for lasing. *Nature materials* **2014**, *13*, 476−480.

(6) Dou, L.; Yang, Y. M.; You, J.; Hong, Z.; Chang, W.-H.; Li, G.; Yang, Y. Solution-processed hybrid perovskite photodetectors with high detectivity. *Nat. Commun.* **2014**, *5*, 5404.

(7) Li, W.; Wang, Z.; Deschler, F.; Gao, S.; Friend, R. H.; Cheetham, A. K. Chemically diverse and multifunctional hybrid organic-inorganic perovskites. *Nature Reviews Materials* **2017**, *2*, 16099.

(8) Braly, I. L.; deQuilettes, D. W.; Pazos-Outón, L. M.; Burke, S.; Ziffer, M. E.; Ginger, D. S.; Hillhouse, H. W. Hybrid perovskite films approaching the radiative limit with over 90% photoluminescence quantum efficiency. *Nat. Photonics* **2018**, *12*, 355−361.

(9) Dong, Q.; Fang, Y.; Shao, Y.; Mulligan, P.; Qiu, J.; Cao, L.; Huang, J. Electron-hole diffusion lengths > ; 175 μm in solution-grown CH3NH3PbI3 single crystals. *Science* **2015**, *347*, 967−970.

(10) Liu, J.; Xue, Y.; Wang, Z.; Xu, Z.-Q.; Zheng, C.; Weber, B.; Song, J.; Wang, Y.; Lu, Y.; Zhang, Y.; Bao, Q. Two-dimensional CH3NH3PbI3 perovskite: synthesis and optoelectronic application. *ACS Nano* **2016**, *10*, 3536−3542.

(11) Blancon, J.-C.; Tsai, H.; Nie, W.; Stoumpos, C. C.; Pedesseau, L.; Katan, C.; Kepenekian, M.; Soe, C. M. M.; Appavoo, K.; Sfeir, M. Y.; Tretiak, S. Extremely efficient internal exciton dissociation through edge states in layered 2D perovskites. *Science* **2017**, *355*, 1288−1292.

(12) Qi, X.; Zhang, Y.; Ou, Q.; Ha, S. T.; Qiu, C.-W.; Zhang, H.; Cheng, Y.-B.; Xiong, Q.; Bao, Q. Photonics and optoelectronics of 2D metal-halide perovskites. *Small* **2018**, *14*, 1800682.

(13) Polavarapu, L.; Nickel, B.; Feldmann, J.; Urban, A. S. Advances in Quantum-Confined Perovskite Nanocrystals for Optoelectronics. *Adv. Energy Mater.* **2017**, *7*, 1700267.

(14) Zhang, Y.; Lim, C.-K.; Dai, Z.; Yu, G.; Haus, J. W.; Zhang, H.; Prasad, P. N. Photonics and optoelectronics using nano-structured hybrid perovskite media and their optical cavities. *Phys. Rep.* **2019**, *795*, 1−51.

(15) Mak, K. F.; Shan, J. Photonics and optoelectronics of 2D semiconductor transition metal dichalcogenides. *Nat. Photonics* **2016**, *10*, 216−226.

(16) Mattinen, M.; Popov, G.; Vehkamaki, M.; King, P. J.; Mizohata, K.; Jalkanen, P.; Raisanen, J.; Leskelä, M.; Ritala, M. Atomic layer deposition of emerging 2d semiconductors, HfS2 and ZrS2, for optoelectronics. *Chem. Mater.* **2019**, *31*, 5713−5724.

(17) Yan, C.; Gan, L.; Zhou, X.; Guo, J.; Huang, W.; Huang, J.; Jin, B.; Xiong, J.; Zhai, T.; Li, Y. Space-confined chemical vapor deposition synthesis of ultrathin HfS2 flakes for optoelectronic application. *Adv. Funct. Mater.* **2017**, *27*, 1702918.

(18) Erkılıc, U.; Solís-Fernández, P.; Ji, H. G.; Shinokita, K.; Lin, Y.-C.; Maruyama, M.; Suenaga, K.; Okada, S.; Matsuda, K.; Ago, H. Vapor phase selective growth of two-dimensional perovskite/WS2 hetero-structures for optoelectronic applications. *ACS Appl. Mater. Interfaces* **2019**, *11*, 40503−40511.

(19) Wang, D.; Zhang, X.; Wang, Z. Recent advances in properties, synthesis and applications of two-dimensional HfS2. *J. Nanosci. Nanotechnol.* **2018**, *18*, 7319−7334.

(20) Zhao, Q.; Guo, Y.; Si, K.; Ren, Z.; Bai, J.; Xu, X. Elastic, electronic, and dielectric properties of bulk and monolayer ZrS2, ZrSe2, HfS2, HfSe2 from van der Waals density-functional theory. *physica status solidi (b)* **2017**, *254*, 1700033.

(21) Kang, J.; Sahin, H.; Peeters, F. M. Mechanical properties of monolayer sulphides: a comparative study between MoS 2, HfS 2 and TiS 3. *Phys. Chem. Chem. Phys.* **2015**, *17*, 27742−27749.

(22) Singh, D.; Gupta, S. K.; Sonvane, Y.; Kumar, A.; Ahuja, R. 2D-HfS 2 as an efficient photocatalyst for water splitting. *Catalysis Science & Technology* **2016**, *6*, 6605−6614.

(23) Singh, D.; Ahuja, R. Enhanced optoelectronic and thermoelectric properties by intrinsic structural defects in monolayer HfS2. *ACS Applied Energy Materials* **2019**, *2*, 6891−6903.

(24) Kumar, C.; Das, S.; Jit, S. *2D Nanoscale Heterostructured Materials*; Elsevier: 2020; pp 195−214, DOI: 10.1016/B978-0-12-817678-8.00007-5.

(25) Guo, Y.; Xue, Y.; Li, X.; Li, C.; Song, H.; Niu, Y.; Liu, H.; Mai, X.; Zhang, J.; Guo, Z. Effects of transition metal substituents on interfacial and electronic structure of CH3NH3PbI3/TiO2 interface: a first-principles comparative study. *Nanomaterials* **2019**, *9*, 966.

(26) Etgar, L.; Gao, P.; Xue, Z.; Peng, Q.; Chandiran, A. K.; Liu, B.; Nazeeruddin, M. K.; Gratzel, M. Mesoscopic CH3NH3PbI3/TiO2 heterojunction solar cells. *J. Am. Chem. Soc.* **2012**, *134*, 17396−17399.

(27) Erkılıç, U.; Solís-Fernández, P.; Ji, H. G.; Shinokita, K.; Lin, Y.-C.; Maruyama, M.; Suenaga, K.; Okada, S.; Matsuda, K.; Ago, H. Vapor phase selective growth of two-dimensional perovskite/WS2 hetero-structures for optoelectronic applications. *ACS Appl. Mater. Interfaces* **2019**, *11*, 40503−40511.

(28) Peng, B.; Yu, G.; Zhao, Y.; Xu, Q.; Xing, G.; Liu, X.; Fu, D.; Liu, B.; Tan, J. R. S.; Tang, W.; Lu, H.; Xie, J.; Deng, L.; Sum, T. C.; Loh, K. P. Achieving ultrafast hole transfer at the monolayer MoS2 and CH3NH3PbI3 perovskite interface by defect engineering. *ACS Nano* **2016**, *10*, 6383−6391.

(29) Liu, Z.; Liu, K.; Zhang, F.; Jain, S. M.; He, T.; Jiang, Y.; Liu, P.; Yang, J.; Liu, H.; Yuan, M. CH3NH3PbI3: MoS2 heterostructure for stable and efficient inverted perovskite solar cell. *Sol. Energy* **2020**, *195*, 436−445.

(30) Fang, Q.; Shang, Q.; Zhao, L.; Wang, R.; Zhang, Z.; Yang, P.; Sui, X.; Qiu, X.; Liu, X.; Zhang, Q.; Zhang, Y. Ultrafast charge transfer in perovskite nanowire/2D transition metal dichalcogenide heterostruc-tures. *journal of physical chemistry letters* **2018**, *9*, 1655−1662.

(31) Ma, C.; Shi, Y.; Hu, W.; Chiu, M.-H.; Liu, Z.; Bera, A.; Li, F.; Wang, H.; Li, L.-J.; Wu, T. Heterostructured WS2/CH3NH3PbI3 photoconductors with suppressed dark current and enhanced photo-detectivity. *Adv. Mater.* **2016**, *28*, 3683−3689.

(32) Kang, D.-H.; Pae, S. R.; Shim, J.; Yoo, G.; Jeon, J.; Leem, J. W.; Yu, J. S.; Lee, S.; Shin, B.; Park, J.-H. An ultrahigh-performance photodetector based on a perovskite-transition-metal-dichalcogenide hybrid structure. *Adv. Mater.* **2016**, *28*, 7799−7806.

(33) Cheng, H.-C.; Wang, G.; Li, D.; He, Q.; Yin, A.; Liu, Y.; Wu, H.; Ding, M.; Huang, Y.; Duan, X. van der Waals heterojunction devices based on organohalide perovskites and two-dimensional materials. *Nano Lett.* **2016**, *16*, 367−373.

(34) Hammer, B.; Hansen, L. B.; Nørskov, J. K. Improved adsorption energetics within density-functional theory using revised Perdew-Burke-Ernzerhof functionals. *Phys. Rev. B* **1999**, *59*, 7413.

(35) Kresse, G.; Furthmüller, J. Efficient iterative schemes for ab initio total-energy calculations using a plane-wave basis set. *Phys. Rev. B* **1996**, *54*, 11169.

(36) Perdew, J. P.; Burke, K.; Ernzerhof, M. Generalized gradient approximation made simple. *Physical review letters* **1996**, *77*, 3865.

(37) Grimme, S.; Antony, J.; Ehrlich, S.; Krieg, H. A consistent and accurate ab initio parametrization of density functional dispersion correction (DFT-D) for the 94 elements H-Pu. *J. Chem. Phys.* **2010**, *132*, 154104.

(38) Paier, J.; Marsman, M.; Hummer, K.; Kresse, G.; Gerber, I. C.; Ángyán, J. G. Screened hybrid density functionals applied to solids. *J. Chem. Phys.* **2006**, *124*, 154709.

(39) Sanville, E.; Kenny, S. D.; Smith, R.; Henkelman, G. Improved grid-based algorithm for Bader charge allocation. *J. Comput. Chem.* **2007**, *28*, 899−908.

(40) Singh, D.; Panda, P. K.; Khossossi, N.; Mishra, Y. K.; Ainane, A.; Ahuja, R. Impact of edge structures on interfacial interactions and efficient visible-light photocatalytic activity of metal-semiconductor hybrid 2D materials. *Catalysis Science & Technology* **2020**, *10*, 3279−3289.

(41) Guo, M.; Yang, Y.; Leng, Y.; Wang, L.; Dong, H.; Liu, H.; Li, W. Edge dominated electronic properties of MoS 2/graphene hybrid 2D materials: edge state, electron coupling and work function. *Journal of Materials Chemistry C* **2017**, *5*, 4845−4851.

(42) Pramchu, S.; Jaroenjittichai, A.; Laosiritaworn, Y. Surface doping of Sn in orthorhombic CH3NH3PbI3 for potential perovskite solar cells: first principles study. *Surf. Coat. Technol.* **2016**, *306*, 285−289.

(43) Brivio, F.; Frost, J. M.; Skelton, J. M.; Jackson, A. J.; Weber, O. J.; Weller, M. T.; Goni, A. R.; Leguy, A. M.; Barnes, P. R.; Walsh, A. Lattice dynamics and vibrational spectra of the orthorhombic, tetragonal, and cubic phases of methylammonium lead iodide. *Phys. Rev. B* **2015**, *92*, 144308.

(44) Hu, W.; Yang, J. Two-dimensional van der Waals heterojunctions for functional materials and devices. *Journal of Materials Chemistry C* **2017**, *5*, 12289−12297.
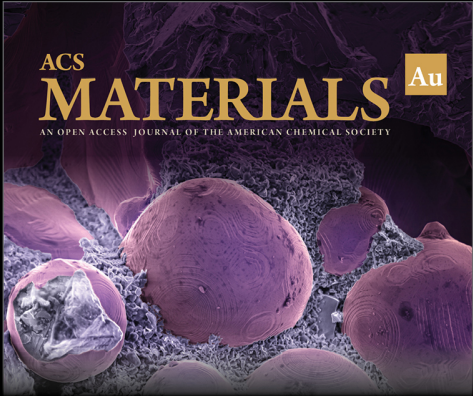
(45) Guo, X.-Z.; Zhang, Y.-D.; Qin, D.; Luo, Y.-H.; Li, D.-M.; Pang, Y.-T.; Meng, Q.-B. Hybrid tandem solar cell for concurrently converting light and heat energy with utilization of full solar spectrum. *J. Power Sources* **2010**, *195*, 7684−7690.

(46) Yadav, A.; Kangsabanik, J.; Singh, N.; Alam, A. Novel Two-Dimensional MA2N4 Materials for Photovoltaic and Spintronic Applications. *J. Phys. Chem. Lett.* **2021**, *12*, 10120−10127.

(47) Chen, Y.; Lao, Z.; Sun, B.; Feng, X.; Redfern, S. A.; Liu, H.; Lv, J.; Wang, H.; Chen, Z. Identifying the ground-state NP sheet through a global structure search in two-dimensional space and its promising high-efficiency photovoltaic properties. *ACS Materials Letters* **2019**, *1*, 375−382.

(48) Wang, Z.; Ganose, A. M.; Niu, C.; Scanlon, D. O. First-principles insights into tin-based two-dimensional hybrid halide perovskites for photovoltaics. *Journal of Materials Chemistry A* **2018**, *6*, 5652−5660.

(49) Wang, Z.; Ganose, A. M.; Niu, C.; Scanlon, D. O. Two-dimensional eclipsed arrangement hybrid perovskites for tunable energy level alignments and photovoltaics. *Journal of Materials Chemistry C* **2019**, *7*, 5139−5147.